Astronomy & Astrophysics manuscript no. huang_resubm
May 16, 2014
©ESO 2014

arXiv:1405.2194v2 [astro-ph.SR] 15 May 2014

Hα spectroscopy and multiwavelength imaging of a solar flare caused by filament eruption

Z. Huang[1,2], M. S. Madjarska[2], K. Koleva[3], J. G. Doyle[2], P. Duchlev[3], M. Dechev[3], and K. Reardon[4]

[1] Shandong Provincial Key Laboratory of Optical Astronomy and Solar-Terrestrial Environment, School of Space Science and Physics, Shandong University (Weihai), 264209 Weihai, Shandong, China
[2] Armagh Observatory, College Hill, Armagh BT61 9DG, N. Ireland
[3] Institute of Astronomy and National Astronomical Observatory, BAS, 72 Tsarigradsko Chaussee blvd., 1784 Sofia, Bulgaria
[4] National Solar Observatory, Sacramento Peak, P.O. Box 62, Sunspot, NM, USA, 88349

Received date, accepted date

ABSTRACT

Context. We study a sequence of eruptive events including filament eruption, a GOES C4.3 flare, and a coronal mass ejection.
Aims. We aim to identify the possible trigger(s) and precursor(s) of the filament destabilisation, investigate flare kernel characteristics, flare ribbons/kernels formation and evolution, study the interrelation of the filament-eruption/flare/coronal-mass-ejection phenomena as part of the integral active-region magnetic field configuration, and determine Hα line profile evolution during the eruptive phenomena.
Methods. Multi-instrument observations are analysed including Hα line profiles, speckle images at H$\alpha-0.8$ Å and H$\alpha+0.8$ Å from IBIS at DST/NSO, EUV images and magnetograms from the SDO, coronagraph images from STEREO, and the X-ray flux observations from FERMI and GOES.
Results. We establish that the filament destabilisation and eruption are the main triggers for the flaring activity. A surge-like event with a circular ribbon in one of the filament footpoints is determined as the possible trigger of the filament destabilisation. Plasma draining in this footpoint is identified as the precursor for the filament eruption. A magnetic flux emergence prior to the filament destabilisation followed by a high rate of flux cancellation of 1.34×10^{16} Mx s^{-1} is found during the flare activity. The flare X-ray lightcurves reveal three phases that are found to be associated with three different ribbons occurring consecutively. A kernel from each ribbon is selected and analysed. The kernel lightcurves and Hα line profiles reveal that the emission increase in the line centre is stronger than that in the line wings. A delay of around 5–6 mins is found between the increase in the line centre and the occurrence of red asymmetry. Only red asymmetry is observed in the ribbons during the impulsive phases. Blue asymmetry is only associated with the dynamic filament.

Key words. Sun: activity - Sun: flare - Sun: filaments - Line: profiles - Methods: imaging and spectroscopy

1. Introduction

Solar flares are powerful solar phenomena that are believed to be driven by magnetic reconnection resulting in plasma heating and particle acceleration. They can be observed as emission enhancements across the entire electromagnetic spectrum, from radio to γ-ray wavelengths. Flares are considered as phenomena initiated in the corona since radio and hard X-ray emission at flaring sites were discovered (Shibata & Magara 2011, and the references therein). For decades, the chromospheric response to flares has been investigated by using Hα filtergrams. Flaring sites observed in Hα show spectacular phenomena such as filament (prominence) eruptions and flare ribbons (bright regions in the chromosphere along the magnetic neutral line); Hα kernels, which are very bright and compact Hα emission sources embedded in flare ribbons, are also common features appearing during a flare. They are believed to be the locations of high-energetic particle precipitation. More details about solar flares can be found in some reviews (e.g. Hudson 2007; Benz 2008; Shibata & Magara 2011; Fletcher et al. 2011, etc.).

Although flares have been observed in chromospheric temperature since the Hα filter was invented in the 1930s, the precise mechanism(s) by which energy release in the corona drives chromospheric emission bursts, called ribbons or kernels, has not been well established. A two-dimensional magnetic reconnection model called CSHKP (Carmichael 1964; Sturrock 1966; Hirayama 1974; Kopp & Pneuman 1976), suggests that the plasma surrounding a null point in the corona is heated such that high coronal pressure, thermal conduction, and non-thermal particles (mostly electrons) can efficiently carry energy from the magnetic reconnection site in the corona to the lower solar atmosphere along the magnetic field lines (Magara et al. 1996). Thermal radiation from soft X-rays, EUV, and UV can also contribute to this process, but this contribution was found to be very small (Allred et al. 2005). Other more recent works have raised questions about the viability of this mechanism in the light of recent observations (Fletcher & Hudson 2008) and suggested Alfvén wave propagation as an alternate energy transport mechanism from the corona to chromosphere during flares (Russell & Fletcher 2013).

Although Hα filtergrams provide a wealth of information on the dynamic morphological evolution of the flare in the chromosphere (Hudson 2007, and references therein), full Hα line profiles have powerful diagnostic potential for understanding the physical mechanism driving solar flares. Based on a static model,

Send offprint requests to: zhu@arm.ac.uk

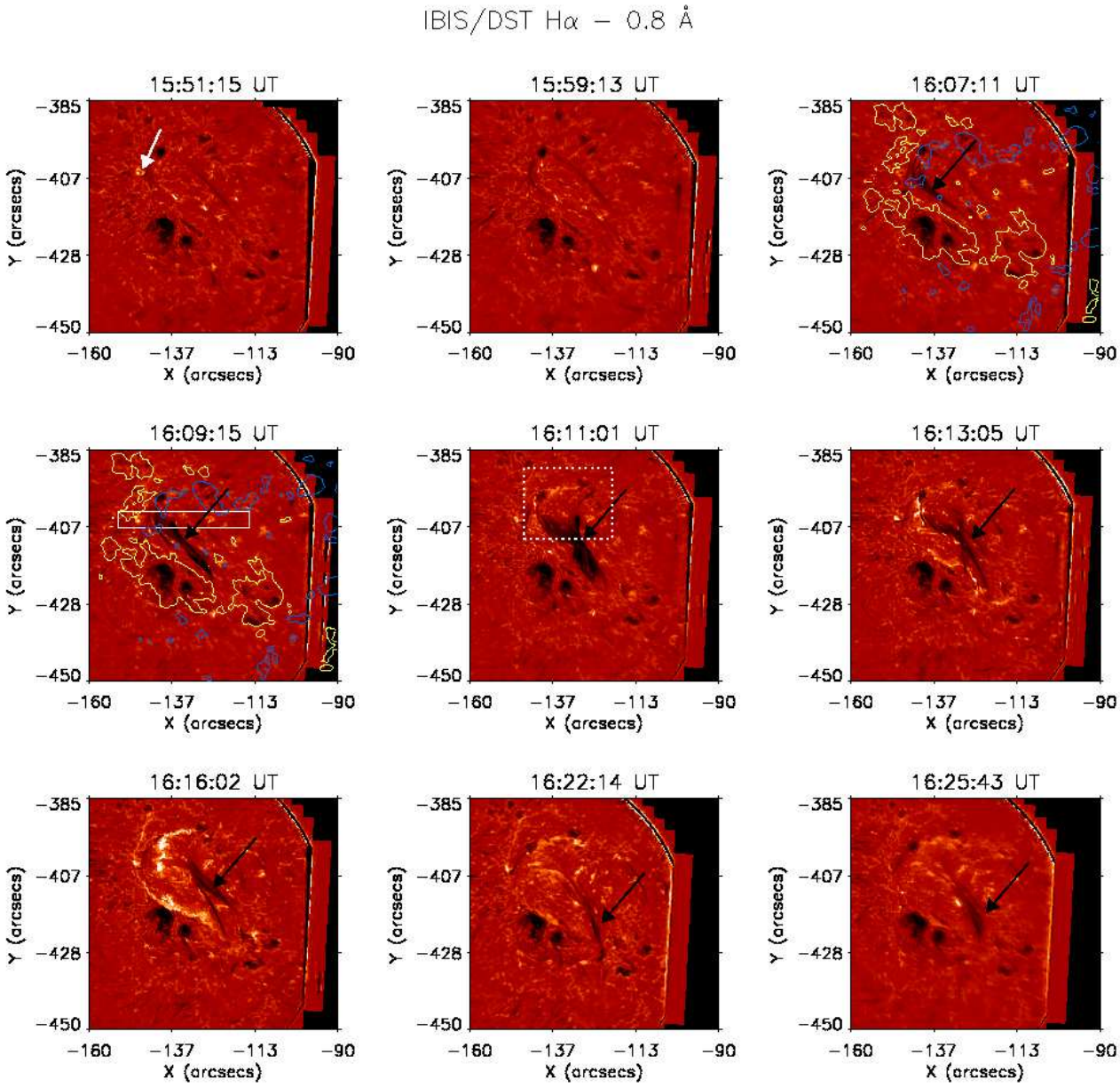

Fig. 1. The filament eruption and the flare ribbon seen in Hα – 0.8 Å. The white arrow at 15:51 UT marks the ribbon associated with the surge-like event in the footpoint of the filament. The black arrows indicate the rising twisted flux-ropes of the filament. The white box at 16:09 UT denotes the region used to produce the slice-time images in Fig. 4. The dotted lines at 16:11 UT denote a region that is enlarged in Fig. 8. Contour plots of HMI magnetogram are shown in images at 16:07:11 UT and 16:09:15 UT (yellow: -300 Mx cm^{-2}, blue: 300 Mx cm^{-2}).

Canfield et al. (1984) calculated Hα profiles of flare chromospheres produced by different mechanisms (see the previous paragraph). They found that central reversal effects on the profiles depend on the heating rate by non-thermal electrons, while increasing thermal conduction reduces the width and total intensity of the profiles, thus lessening the contribution to the flare Hα enhancement. They pointed out that a high coronal pressure can dramatically enhance the width and total intensity of the Hα line and only a high value of non-thermal electron flux can produce Hα profiles with non-Gaussian broad wings. Fang et al. (1993) also considered the non-thermal excitation and ionisation effect in the flare and suggested that bombardment of the non-thermal electrons in the chromosphere can also significantly strengthen and broaden Hα profiles. However, the detection of the effect of non-thermal electron beams on Hα profiles is still under debate. Kašparová et al. (2009) concluded from their simulations that the non-thermal electron beams generally result in emission enhancement although they can also affect the line wings. It is generally accepted that different heating mechanisms most probably work together (e.g. Saint-Hilaire & Benz 2005; Cheng et al. 2006).

Enhanced emission in the red wing of the Hα line, or a line-wing bisector that shifts more towards the red, are often observed in flare kernels. This feature is called a “red asymmetry” (Švestka 1976, and references therein). Red asymmetry is considered to be a signature of downward-moving chromospheric material which results from cooling and condensation of the chromospheric material previously heated during “chro-

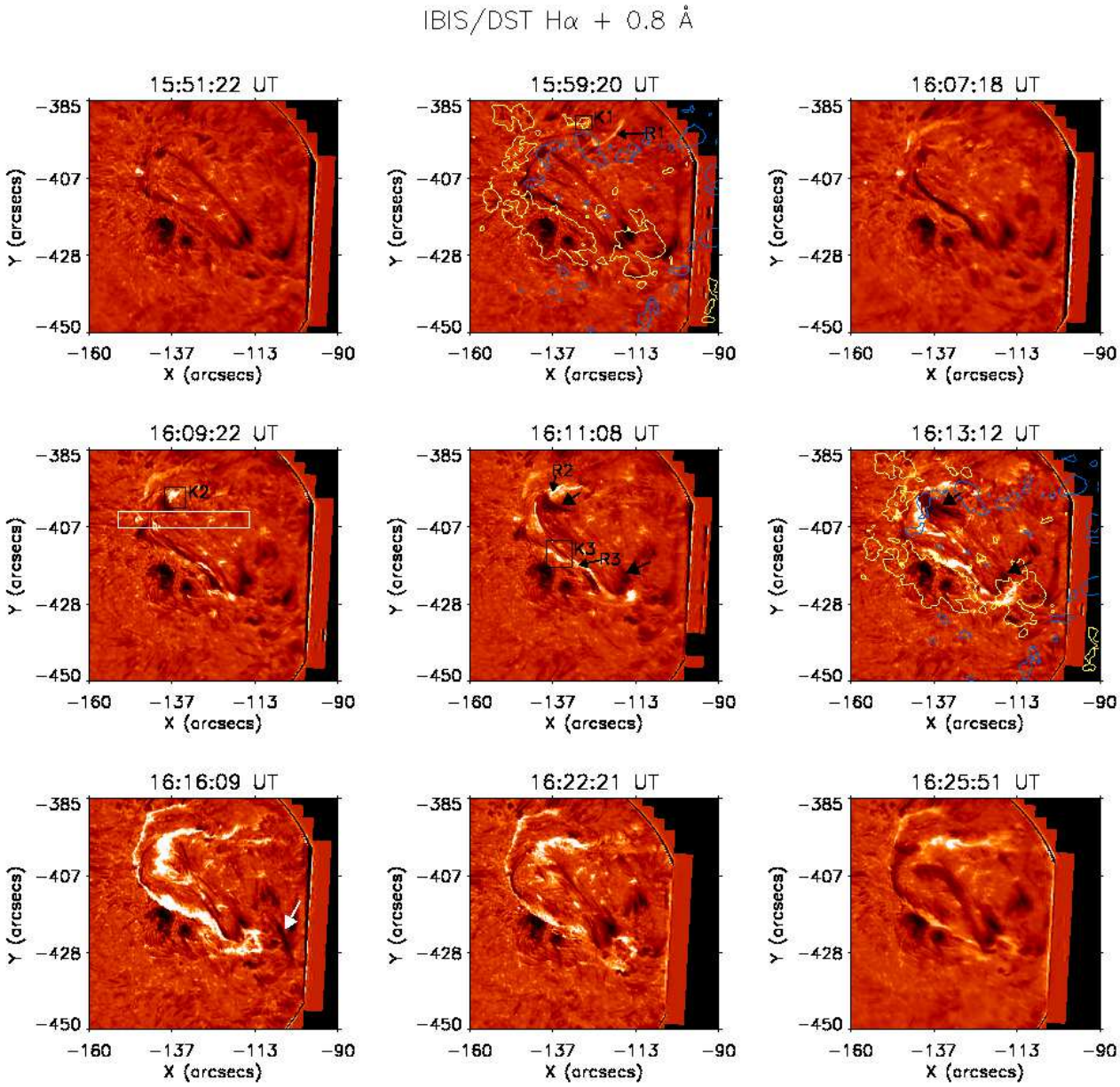

Fig. 2. The filament eruption and the flare ribbon seen in Hα+ 0.8 Å. Larger black arrows indicate the footpoints of the filament where down-flows are observed (at 16:11 UT). Three kernels (K1, K2, and K3) are noted on the images at 15:59 UT, 16:09 UT, and 16:11 UT, respectively. The ribbons (R1, R2, and R2) are shown with arrows in the images at 15:59 UT and 16:11 UT. The white box in the image at 16:09 UT indicates the region used to produce the time-slice plot in Fig. 4. The white arrow at 16:16:09 UT marks the top of the falling back filament ropes (or part of it). Contour plots of HMI magnetogram are shown in images at 16:07:11 UT and 16:09:15 UT (yellow: -300 Mx cm^{-2}, blue: 300 Mx cm^{-2}).

mospheric evaporation". The term chromospheric evaporation refers to the process of the dense, cold chromospheric plasma being heated to tens of million degrees by the energy released during the solar flare in the corona, and its subsequent expansion up into the corona (Zarro et al. 1988; Canfield et al. 1990a,b). Various authors (e.g. Ichimoto & Kurokawa 1984) have found that Hα kernels exhibiting red asymmetry are very small ($< 1''$) and change position continuously. The lifetime of the red asymmetry is shorter than that of the kernel. It has been reported that red asymmetry can be seen in many parts of the flare ribbons in most flares (Tang 1983; Ichimoto & Kurokawa 1984; Canfield et al. 1990b). Recently, Asai et al. (2012) found that the red asymmetry appears all over the flare ribbons with the strongest red asymmetry located on the outer narrow edges of the flare ribbons (with a width of $1.5''-3''$) where the strongest energy release occurs. Deng et al. (2013) found that red asymmetry is observed only in the core area of the flare ribbons during the impulsive phase.

A different (or opposite) phenomenon, "blue asymmetry", is also found in the early stages of the impulsive phase (e.g. Švestka et al. 1962; Tang 1983; Canfield et al. 1990b; Graeter & Kucera 1992; Ji et al. 1994, etc). However, observations of blue asymmetry are somewhat controversial and different mechanisms have been proposed (Heinzel et al. 1994). They have been associated with chromospheric evaporation (Hirayama 1974) and electron beam heating with return cur-

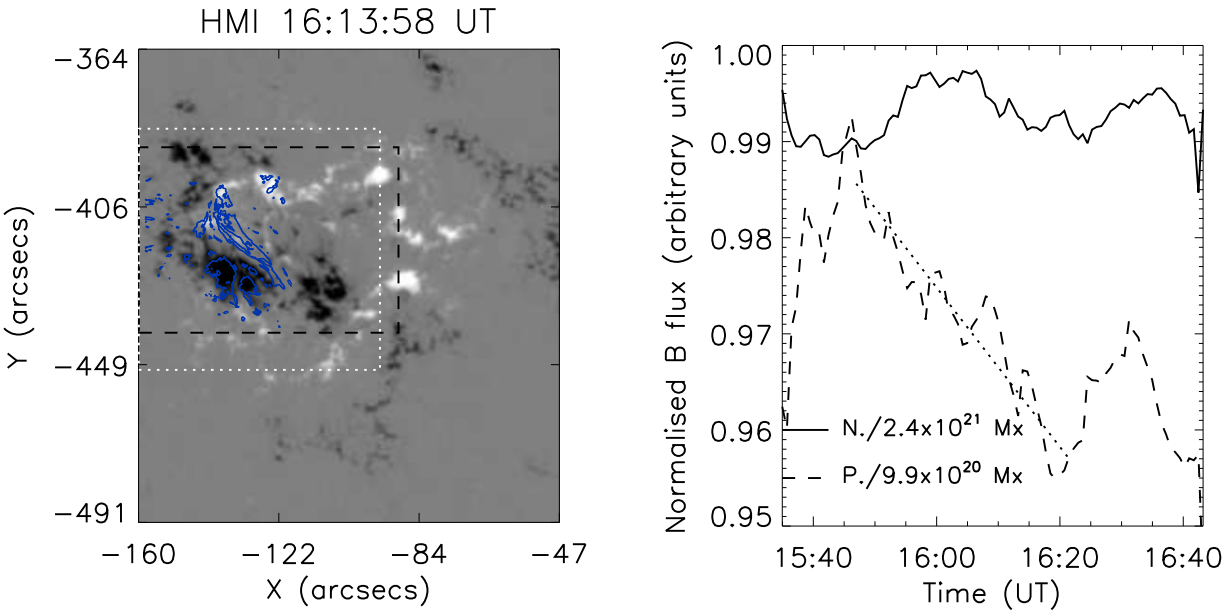

Fig. 3. Left: HMI longitudinal magnetogram of the flare scaled from -1 kG to 1 kG. The region enclosed with dotted lines is the IBIS field of view. The overplotted contours (blue lines) outline the filament and two of the sunspots in the flaring region. **Right:** lightcurves of the normalised (to the maximum) magnetic flux from the region shown with black dashed line in the left panel. The solid line indicates the variation of the negative flux while the dashed line is the positive one. The cancellation rate of the positive flux is obtained from the linear fit of the positive flux lightcurve shown here with a dotted straight line.

rents (Heinzel et al. 1994). Ji et al. (1994) argue that blue asymmetry is an observational effect from multiple evolving loops. Ichimoto & Kurokawa (1984) found a momentum balance between the downward motion of the chromospheric condensation and the chromospheric evaporation, thus confirming that the red asymmetry is a counteraction of the chromospheric evaporation. In some cases, both red and blue asymmetry can be found in the same flare (Canfield et al. 1990b). These authors found blue asymmetry associated with eruptive and untwisting filaments in one case, and suggested that two other cases are related to unresolved filament activation occurring at a very small spatial scale.

Eruptive prominences (EPs) or filaments are frequently associated with coronal mass ejections (CMEs) and flares (Tandberg-Hanssen 1995). All three phenomena occur in the same large-scale magnetic field configuration, but the precise relationship between these phenomena has not yet been clearly established. Hence, an investigation of the complex trio phenomenon (filament eruption/flare/CME) observed at high-spatial and temporal resolution from the chromosphere to the corona is essential for understanding the physical mechanism(s) driving each of these events.

Triggers of prominence eruption are under debate, with various mechanisms being discussed and modelled during the past few decades (see review by Chen 2011, and the references therein). It has been suggested that new emerging magnetic flux (which reconnects with the preexisting field) in the vicinity of a filament can trigger destabilisation of a filament (Feynman & Martin 1995). Indeed, Canfield & Reardon (1998) observed the emergence of flux with signatures of twist which injected that twisted magnetic field into the filament, leading to its destabilisation and eruption. The precursors of filament eruptions can be viewed as the key to understanding the physical mechanisms responsible for the destabilisation and eruptions. Martin (1980) reviews the primary signatures of the pre-flare phase of filament eruptions among which are: increased absorption in the blue/red wing and line centre as early as 30 min prior to the eruption, transition from absorption to emission of the prominence plasma in transition region and coronal lines, and complete or partial disappearance in Hα suggesting a heating process. Many precursors have been found by different authors, for example, plasma drainage from the prominence to the chromosphere (Tandberg-Hanssen 1995; Gilbert et al. 2000), heating of filament plasma before (Cirigliano et al. 2004; Kucera & Landi 2006) and during eruptions (Engvold et al. 2001; Kucera & Landi 2008), a cavity size increase (Gibson et al. 2006), darkening or brightening of parts of the filament body or its close vicinity in high temperature EUV lines (Alexander et al. 2006), and an X-ray brightening in the vicinity of the filament (Harrison et al. 1985).

There have been numerous reports on solar flares and associated processes like eruptive filaments and CMEs. Here, we report the observations of an active region near disk centre from the chromosphere (spectroscopically and imaging) through the transition region and corona (imaging). We make an in-depth spectroscopic and imaging analysis of the complex filament eruption/flare/CME phenomenon using space- and ground-based observations with largely unprecedented temporal and spatial resolution covering the entire solar atmosphere from the chromosphere to the corona. We study the trigger and filament-eruption precursors, analyse the Hα profile searching for the mechanism producing chromospheric flare emission bursts, investigate the time evolution of red- and blue asymmetries and the phenomena causing their occurrence, analyse the magnetic flux evolution, and examine the formation of the coronal mass ejection with respect to the filament/flare events as they unfold. In Section 2 of the article we describe the observations. Section 3 presents the results and discussion of the filament eruption (Section 3.1), flare evolution (Section 3.2), the Hα spectroscopy study (Section 3.3), magnetic field evolution (Section 3.4), and the CME association (Section 3.5). The obtained results are summarised in Section 4.

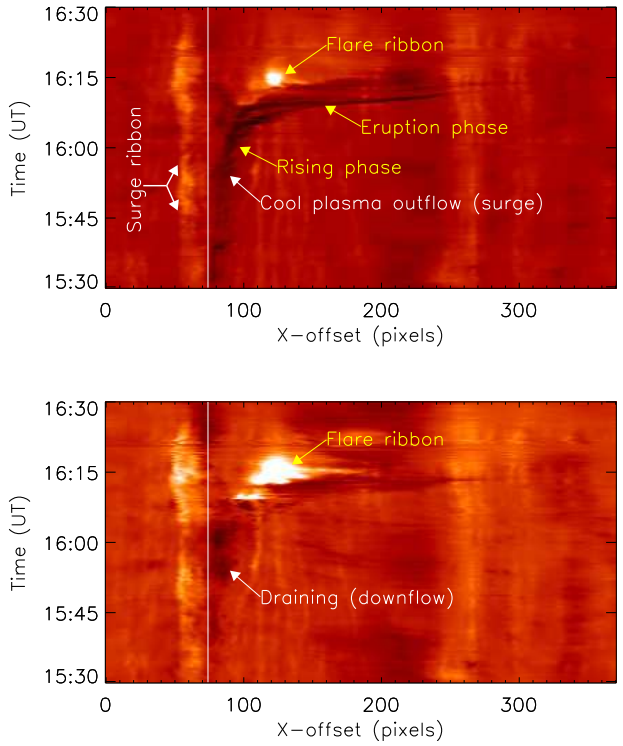

Fig. 4. Top: Time-slice image in Hα – 0.8 Å showing the ribbon associated with the surge-like event, the rising filament, and its eruption as a dark feature. **Bottom:** Hα + 0.8 Å time-slice image showing plasma draining in the filament footpoint. The arrows indicate all identified phenomena, i.e. surge-like down-flow (draining of cool material) and the flare's ribbon. The slice was taken at the location indicated with a white box in Figs. 1 and 2.

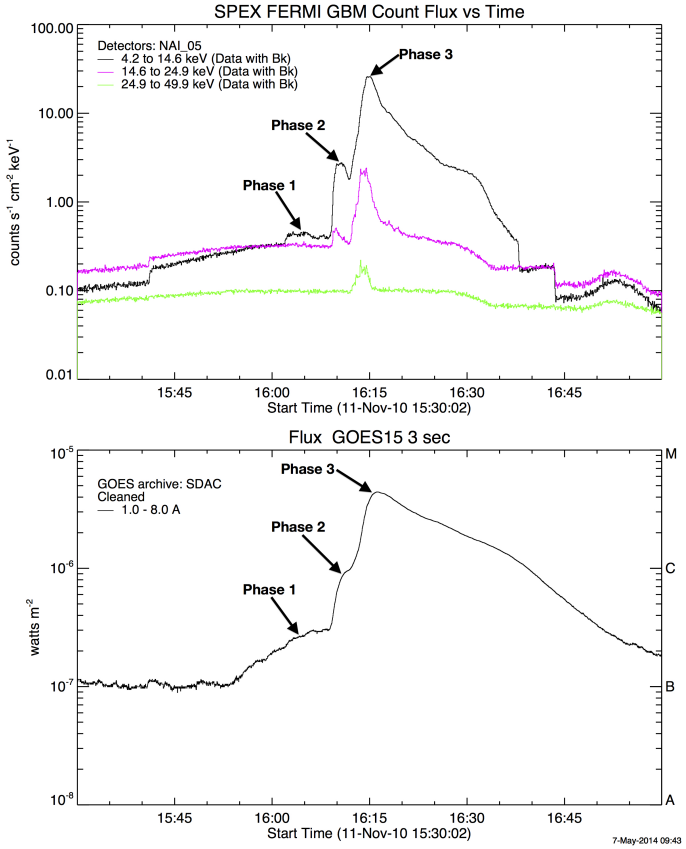

Fig. 5. The solar X-ray flux measured by FERMI (top) and GOES (bottom). The arrows indicate the three impulsive peaks.

2. Observations

Our dedicated Hinode/Dunn Solar Telescope (DST) observing campaign took place from 2010 November 10 to 18. On November 11 we targeted NOAA 11123, a complex $\beta\gamma$ active region composed of eight sunspots, and observations were taken in the time interval from 15:14 UT to 17:08 UT. The active region produced five GOES C class flares with the strongest of GOES class C4.7. Unfortunately, Hinode was not targeting the active region, so we do not have crucial information from the three Hinode instruments. Nevertheless, unique observations of this flare were taken with several instruments from ground- and space-based observatories. We used data from the Interferometric BIdimensional Spectrometer (IBIS, Cavallini 2006) mounted on the DST at the National Solar Observatory (NSO) at Sacramento Peak which is equipped with a high-order adaptive optics system. The space-based instruments include the Atmospheric Imaging Assembly (AIA) and the Helioseismic and Magnetic Imager (HMI) on board the Solar Dynamics Observatory (SDO), the Extreme Ultraviolet Imager (EUVI) and COR1 inner coronagraph on board the Solar Terrestrial Relations Observatory (STEREO) Behind (B) and Ahead (A) spacecraft, the Gamma-ray Burst Monitor (GBM) on board FERMI and the Geostationary Operational Environmental Satellite (GOES). A GOES C4.3 flare was registered by all instruments starting at 15:54 UT together with a filament eruption followed by a coronal mass ejection recorded by LASCO/SoHO and COR1/COR2/SECCHI/STEREO A and B. A description of the instruments that were used together with details on the obtained data and their reduction are given below.

2.1. IBIS

IBIS uses a pair of Fabry-Perot interferometers to record very narrow-band filtergrams in the spectral range 5800–8600 Å (Cavallini 2006; Reardon & Cavallini 2008). It has a 95″ diameter circle field of view and a pixel size of about 0.1″. Please note that we study the flare in a 65″ x 65″ area that was cut from the IBIS circular field of view. The observations were taken in the Hα 6562.8 Å line. A sequence of data segments was specially designed to obtain both full spectral scan and seeing-free images at two selected wavelengths at the highest possible cadence. For each data segment, IBIS first scanned the Hα line from −1.4 Å to +1.4 Å centred on the line centre with a 0.2 Å step for a total of 15 points, followed by 50 images taken at a fixed wavelength at 6562 Å (i.e. Hα – 0.8 Å), and then 50 images at 6563.6 Å (i.e. Hα+0.8 Å). We named the images taken at a fixed wavelength "speckle stacks". The frame rate was about 5 frames per second and the exposure time was 35 ms. The full sequence was repeated every 17 s. Before the science observations, IBIS took a dataset by scanning the Hα line profile from Hα – 2.0 Å to Hα + 2.0 Å with about 36 mÅ per step, which was used for pre-filter correction. A dataset for dark-current calibration was taken with the sunlight blocked, and a dataset for flat-field correction was obtained at the same wavelengths as the line-scan data.

The data reduction is different for line-scan and speckle stack data. For the line-scan data, the calibration includes dark-current, flat-field, blue-shift, pre-filter, and destretching corrections (see e.g. Cauzzi et al. 2009, for details). For the speckle stack, the dark-current and flat-field corrections are first performed, then

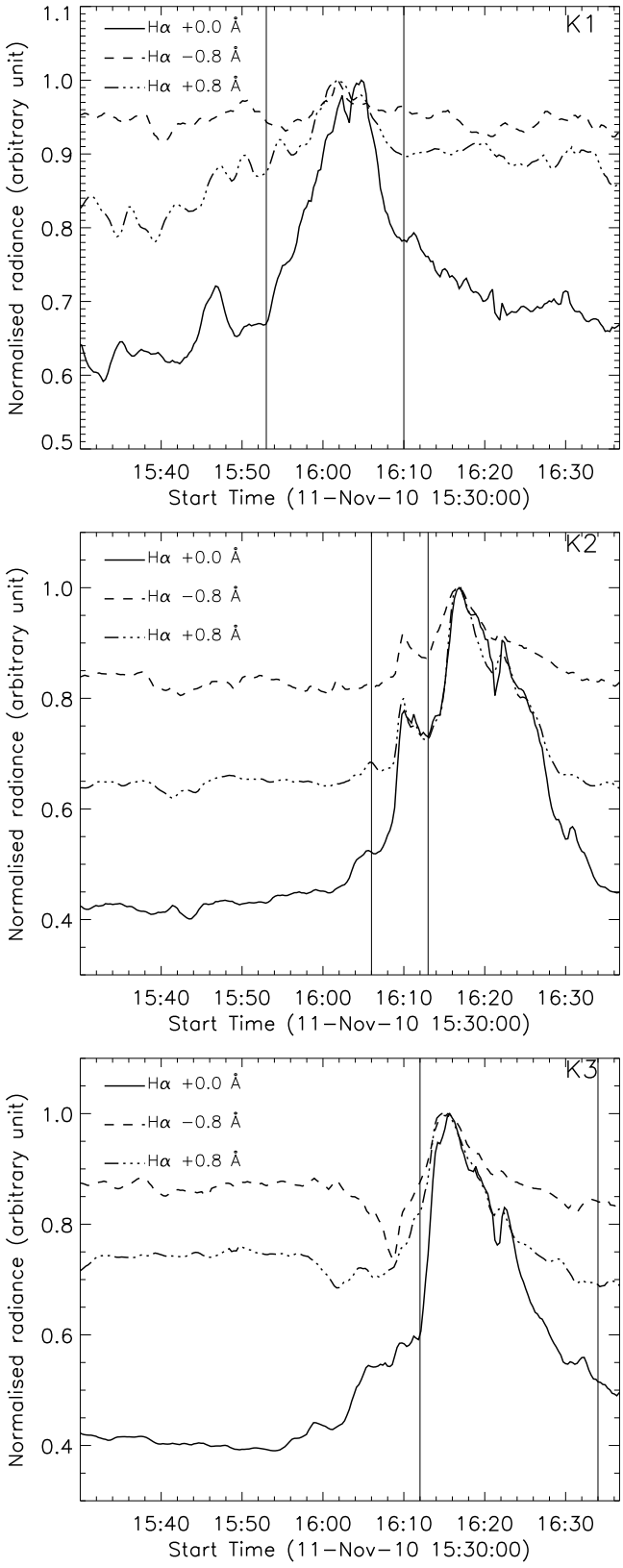

Fig. 6. Lightcurves of the flare kernels outlined with boxes in Figure 2 in the Hα line centre, Hα – 0.8 Å, and Hα + 0.8 Å. The vertical lines indicate the onset time of each kernel occurrence. Top: K1; middle: K2; bottom: K3.

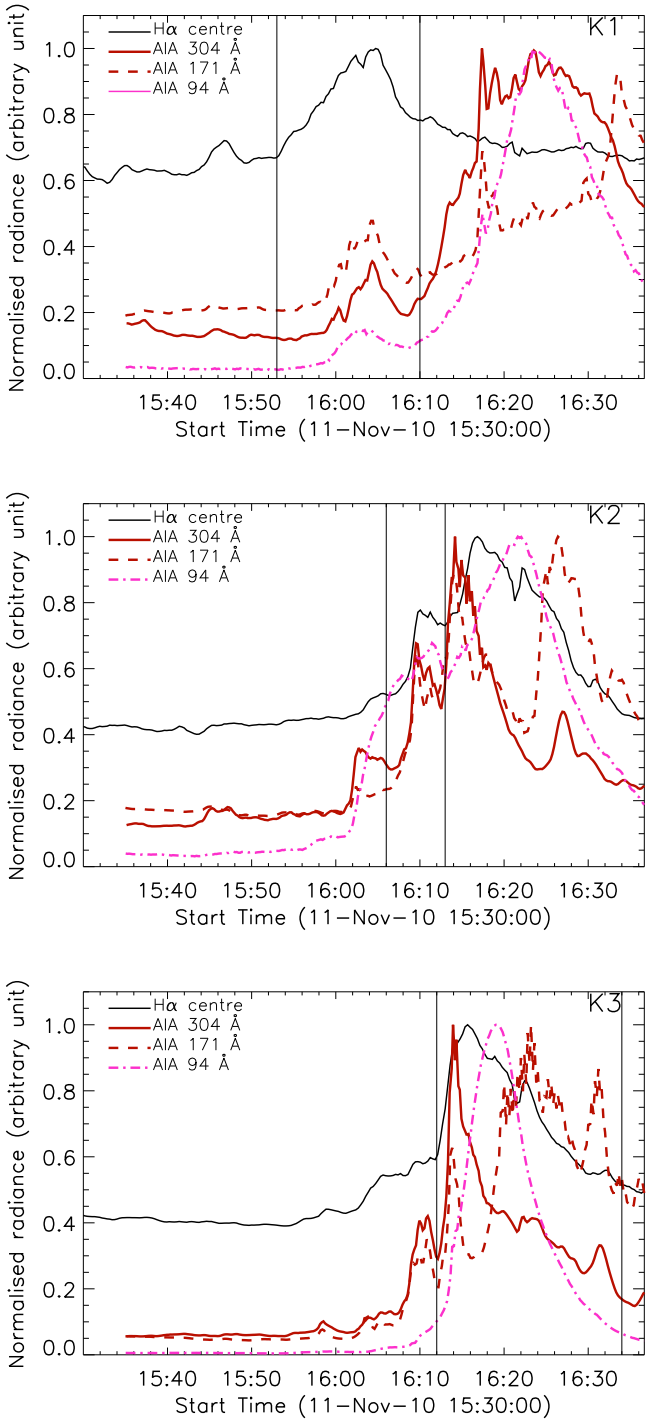

Fig. 7. Lightcurves of the flare kernels outlined with boxes in Fig. 2 in the AIA 304 Å, 171 Å, and 94 Å channels, and the corresponding Hα line centre lightcurves are overplotted for reference. The vertical lines indicate the onset time of each kernel occurrence. Top: K1; middle: K2; bottom: K3.

each speckle stack (50 images) is used as input to an imaging reconstruction package called the Kiepenheuer-Institut Speckle Interferometry Package (KISIP, Wöger et al. 2008, and references therein) to produce a single output image. The KISIP package is designed to reconstruct solar speckle interferometric data observed using an AO system (Wöger et al. 2008). The image reconstruction improves the quality of the images that were blurred owing to the turbulent atmospheric conditions. After this calibration process, each data segment consists of a line-scan image,

Table 1. Timeline of the filament-eruption/flare/CME activities.

Time (UT)	Filament activities	Flare activities			CME
		X-ray	Hα	EUV	
15:45	Circular ribbon and surge-like activity				
15:53	Filament starts slowly rising		Hα line centre of K1 starts rising		
15:58			Red asymmetry in K1 starts		
15:59	Filament eruption starts				
16:02		Peak of the 1st impulsive phase	Peak of K1 Hα line centre intensity	Peaks of the K1 EUV lightcurves (LCs)	
16:03			Line centre in K2 starts rising		
16:05			Line centre in K3 starts rising		
16:08			Red asymmetry in K2 starts		
16:10	Full eruptive phase of the filament	Peak of the 2nd impulsive phase	Peak of K2 Hα line centre intensity	Peaks of the K2 of AIA 304 Å and 171 Å LCs	
16:11			Red asymmetry in K3 starts		
16:13				Peak of the K2 AIA 94 Å LC	
16:14 to 16:15		Peak of the 3rd impulsive phase	Peak of K3 Hα line centre intensity	Peaks of the K3 AIA 304 Å and 171 Å LCs	First CME cloud in COR1
16:16	Falling back of filament material observed				
16:19				Peak of the K3 AIA 94 Å LC	
16:25 to 16:30					Second CME cloud in COR1

one image at Hα – 0.8 Å, and one image at Hα + 0.8 Å at a cadence of 17 s.

2.2. AIA/HMI/SDO

We analysed data from AIA (Lemen et al. 2012) and HMI (Schou et al. 2012) on board SDO (Pesnell et al. 2012). The AIA data used here were taken in the 1600 Å, 304 Å, 171 Å, 193 Å, and 94 Å passbands at 12 s cadence and exposure time that varies during the flare. The response of these channels to different temperature plasma can be found in O'Dwyer et al. (2010). The HMI measures Doppler shifts, intensity, and vector magnetic field using the Fe I 6173 Å absorption line. For the present study only the longitudinal magnetograms were analysed. The AIA images have a pixel size of 0.6″. The HMI magnetograms have a pixel size of 0.505″, a cadence of 45 s, and a 1σ noise level of 10 G (Liu et al. 2012).

2.3. Fermi

Data from GBM (Meegan et al. 2009) on board the *Fermi* mission were also analysed for this study. The GBM has 12 sodium iodide (NaI) detectors which cover the energy range from 8 keV to 1 MeV and two bismuth germanate (BGO) detectors covering the range from 200 keV to 40 MeV. The detectors are positioned on the side of the spacecraft in order to view the part of the sky not obscured by the Earth. In this paper we use data only from the sun-ward oriented NaI detector labeled n5. For this flare only the CSPEC (Continuous Spectroscopy) data were available; CSPEC has 128 energy channels that take data at 4.096 s nominal time resolution, which can change to 1.024 s (trigger mode) if a sufficient count rate is reached.

2.4. EUVI/COR1/STEREO

We analysed observations from the EUVI (Howard et al. 2008) and the COR1 inner coronagraph on board STEREO-B and A (Kaiser et al. 2008). EUVI has a field of view of 1.7 $R_\odot$ and observes in four spectral channels, He II 304 Å, Fe IX/X 171 Å, Fe XII 195 Å, and Fe XIV 284 Å, that cover the 0.1 MK to 20 MK temperature range. The EUVI detectors have a 2048×2048 pixel^2 field-of-view with a pixel size of 1.6″. In the present study, we used images in the He II 304 Å and Fe IX/X 193 Å channels with an average cadence of 10 min and 2 min, respectively. COR1 is

a classic Lyot, internally occulting, refractive coronagraph with a field of view from 1.3 to 4 solar radii. The separation angle between the two satellites (A) and (B) on 2010 November 11 was 167.412°, and the separation angles with Earth were +84.5° for A and -82.9° for B.

The co-alignment of all data is made by aligning images covering similar temperature ranges. The white-light images taken by SDO/AIA and DST were used as references when it was required.

3. Results and Discussion

The combination of ground and space-based observations described above provide a nearly unique view of a filament eruption, flare, and CME, and the complex evolution of the solar chromosphere, transition region, and corona during these impulsive processes. The flare that occurred during our observations was classed as GOES C4.3. We describe in detail the triplet of activity in the following subsections, while a general timeline can be found in Table 1. The spatial relation among the magnetic polarities, flare ribbons, and filament (including its legs) can be obtained from Figs. 1, 2, and 3.

3.1. Filament eruption

One of the main goals of the present study was to identify the possible trigger(s) and precursor(s) of the filament destabilisation. From the visual analysis of the speckle blue- and red-wing images (Figs. 1 and 2) taken at Hα±0.8 Å we identified an increased activity in one of the feet of the prominence. If we interpret the increased absorption in the wings as a Doppler velocity signature, it appears that cool material is rising and draining along one of the filament legs (see the region noted by a white arrow at 15:51:15 UT in Fig. 1). While the up-flow lasted only approximately 5 mins, the plasma draining persisted for almost 10 mins and was followed by a slow ascent and then an abrupt eruption of the filament. A circle ribbon at the filament footpoint together with simultaneous rising and falling material seen as increased absorption in the blue and red wings, strongly suggests a surge-like activity occurring at this location. Unfortunately, we are not able to determine the trigger for the surge-like activity. The HMI resolution (0.505″ pixel size) is five times lower than the IBIS resolution (0.1″) and this does not permit us to identify the small-scale magnetic flux changes in the footpoint of the surge-like phenomenon. The size of this footpoint is ∼3 arcsecs. Magnetic flux emergence is believed to be the trigger for a surge formation (Jiang et al. 2007), but so far it has been studied only for larger events because of resolution constraints. Line-of-sight effects prevent us from establishing whether the ribbon is related to the flows in the footpoint or if a separate surge-like event at the filament footpoint takes place. The timeline of the events is given below.

The dynamic evolution of the region showed a sharp brightness increase in the circular ribbon at ≈15:45 UT which is also the time when the up- and down-flows of cool plasma started in the filament footpoint. Plasma draining in filament footpoints (often in just one foot) is a typical precursor for filament destabilisation (see Section 1 for more details). In addition, the analysis of the total magnetic flux (integrated over the active region area outlined with a black dashed line in the left panel of Fig. 3) in the HMI longitudinal magnetograms clearly shows an abrupt increase in around 3% of the positive flux in just 10 mins. The integrated flux reaches its maximum by the time the first sign of destabilisation was recorded and then sharply decreases during the duration of the filament-eruption and flare activity (Fig. 3). The change in the magnetic field will be discussed later in Sect. 3.4. The filament eruption started at 15:59 UT with a transverse component of the rise velocity of 8 km s^{-1}. During the eruption phase, the velocity (estimated from the time-slice plots) increased from 36 km s^{-1} to 85 km s^{-1} from 16:09 UT to 16:16 UT. We note that while the whole filament rose, only part of it, approximately one quarter appears to have erupted. We cannot conclude with certainty whether this filament eruption can be classified as partial (with some of the material that escapes with the CME) or failed. We clearly see that part of the filament falls back (see the white arrow in Fig. 2 at 16:16:09 UT pointing at the down-falling filament material, and animation Fig. A.4 online), but we cannot reject the possibility that some of the prominence material made it into the coronal mass ejection (CME; see Section 3.5). The filament rise and fall are also seen in emission in all AIA channels shown in Figs. 9, 10, and 11 as well as the animated material given online (Fig. A.4). The erupting filament seen in emission in these channels suggests heating to temperatures as high as $logT(K) = 5.8$. We note that the 171 Å and 304 Å channels have a significant contribution from cooler emission (for details see Del Zanna et al. 2011), which could explain the appearance of the cooler prominence material in these passbands. There is a clear indication that the erupting filament pushed into the overlying loops which then erupted as part of the CME (see the animation online Fig. A.4). A 2π twist of the filament is clearly visible while rising, best seen in Hα–0.8 Å at 16:11 UT (Fig. 1). The time-slice plots shown in Fig. 4 are produced by cutting through the surge-like event to illustrate the sequence of events described above.

3.2. Flare evolution

The multi-instrument approach of the present analysis was crucial for untangling the complexity of the filament–flare activity. We especially took advantage of the high-cadence and high-resolution imaging and spectroscopy of these events in order to investigate in great detail their temporal and spatial evolution at small scale. As we discussed above, the Hα observations clearly indicated that the flare was triggered by the filament destabilisation and eruption. The GBM/Fermi lightcurves (Fig. 5) point towards three phases of the flare evolution before the decay phase, each with different energetics. We were able to determine the events that relate to each of these phases by combining temporally and spatially the chromospheric, EUV soft X-ray, and hard X-ray observations. We identified the formation of three flare ribbons (noted as R1, R2, and R3 in Fig. 2) which occur consecutively during these phases. All three ribbons are clearly seen in the Hα blue and red wings with a stronger presence in the red wing (as discussed in detail in Section 3.3). We selected and analysed in detail three chromospheric kernels, one from each ribbon, and discuss them in detail together with their corresponding coronal activity. The kernels are shown with boxes in Fig. 2 (red wing of Hα) and Fig. 10 (AIA 171 channel) and are labeled as K1, K2, and K3. The kernels corresponding to the lightcurves in Hα and AIA EUV channels are given in Figs. 6 and 7. The box sizes were chosen to include the moving kernel during its evolution (see Section 1 on kernel characteristics).

K1: Kernel K1 belongs to the flare ribbon which initially appeared in the active region during the first phase (from approximately 16:00 UT to 16:09 UT). The lightcurves of the kernel

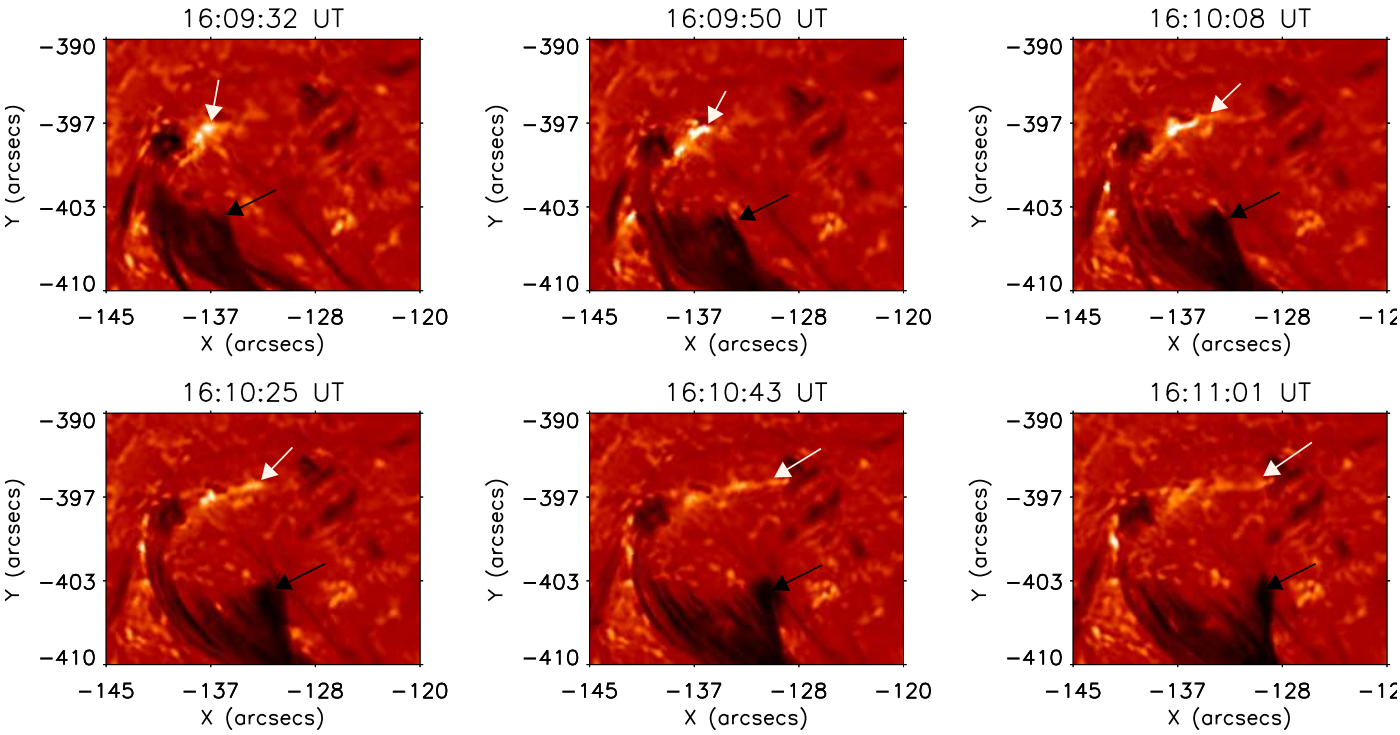

Fig. 8. Hα blue wing images enlarged from the region denoted as dotted lines in Fig. 1 at 16:11 UT. The arrows indicate the location in each image of the rising filament (black) and simultaneously forming ribbon (white) in its upper footpoint.

in the Hα wings and line centre are shown in Fig. 6, top panel. Please note that the speckle images (at Hα±0.8 Å) were used to produce the wing lightcurves in order to take advantage of the better spatial resolution and stability of these images. The lightcurves reveal that the most significant increase in the emission is recorded in the line centre while the wing's response is much weaker and shorter in time.

The intensity peak in this kernel is at approximately 16:02 UT and lasts until 16:06 UT. It reflects the chromospheric response to the coronal activity which started as early as 15:44:36 UT in AIA 171 Å, 15:44:43 UT in AIA 193 Å, and 15:45:44 UT in AIA 304 Å (see the animation online Fig. A.4). This flare precursor activity slows down for a few minutes and then takes off quickly at ~15:54 UT. Its location is shown with a white arrow in Figs. 9 – 11 at 15:59 UT. A small-brightening in the corona at the junction of two loop systems with different orientations can be seen at this time that produces a significant peak in the coronal emission at around 16:02 UT (top panel of 7). A rising loop is seen clearly after 16:06 UT (see the arrows at 16:07 UT in Figs. 9 – 11 and the animation in Fig. A.4). The coronal activity results in a weak two-ribbon formation which can be clearly seen in the image in Fig. 2 at 15:59:20 UT where kernel K1 was also found. A slight increase in the hard X-ray emission is detected by the GBM detectors in the energy channel from 4.2 keV to 14.6 keV shortly after 16:00 UT which lasts until around 16:09 UT. In addition, a weak emission increase is also noticeable in the GOES soft X-ray detector in the range of 1.0 – 8.0 Å (see Fig. 5).

K2: Kernel K2 was formed as part of the ribbon that appears while the filament is rising up during the second phase. The corresponding lightcurves are shown in Figs. 6 and 7, middle panels. The kernel is first seen in the line centre while the signature in the blue and red wings is recorded for a much shorter period of time. As in K1, the increase of the Hα emission in the line centre dominates the relative intensity increase in the wings. A stronger red asymmetry is also observed (for more details on the asymmetry see the next section). The Hα emission starts to increase sharply after 16:09 UT reaching its maximum at 16:10 UT. The same evolution is seen in the EUV emission (Fig. 7, middle panel). We note that while the AIA 304 Å and 171 Å channels peak at the same time as the Hα line centre, the 94 Å response is almost 3 mins later. The most plausible explanation is that this channel is dominated by emission from higher temperature plasma (mainly from Fe XVIII logT~6.8 K and some from Fe XX logT~7.0 K) while the other two channels record mostly cooler transition region and coronal plasma (logT~4.7 K and 5.9 K). The AIA 304 Å and 171 Å channels may pick up footpoint emission due to non-thermal electrons. Therefore, the response in these channels may precede that in the AIA 94 Å channel which represents emission from the loop top due to chromospheric evaporation. In Fig. 8 we show a series of images that clearly demonstrate how the ribbon forms while the filament footpoint makes a lateral movement. This evolution can also be followed in the online material (Fig. A.4). There is little doubt that the reconnection in the corona is triggered by the rising and expanding filament pushing the overlying coronal structures. The timing of these events coincides clearly with the eruption phase of the filament which starts at ~16:09 UT (see Section 3.1). A second sharp increase in the hard (GBM) and soft (GOES) X-ray emission starts just before 16:09 UT and reaches peak emission at ~16:10 UT. During this phase, GBM/Fermi records hard X-ray emission in both channels: 4.2 keV to 14.6 keV and 14.6 keV to 24.9 keV. The next peak in the intensity curve in this kernel comes from the major flare which reaches a maximum at 16:15 UT.

K3: The K3 kernel (Figs. 6 and 7, bottom panels) is part of the large ribbon resulting from the strongest energy release during the third phase. The Hα and the AIA 304 Å and 171 Å

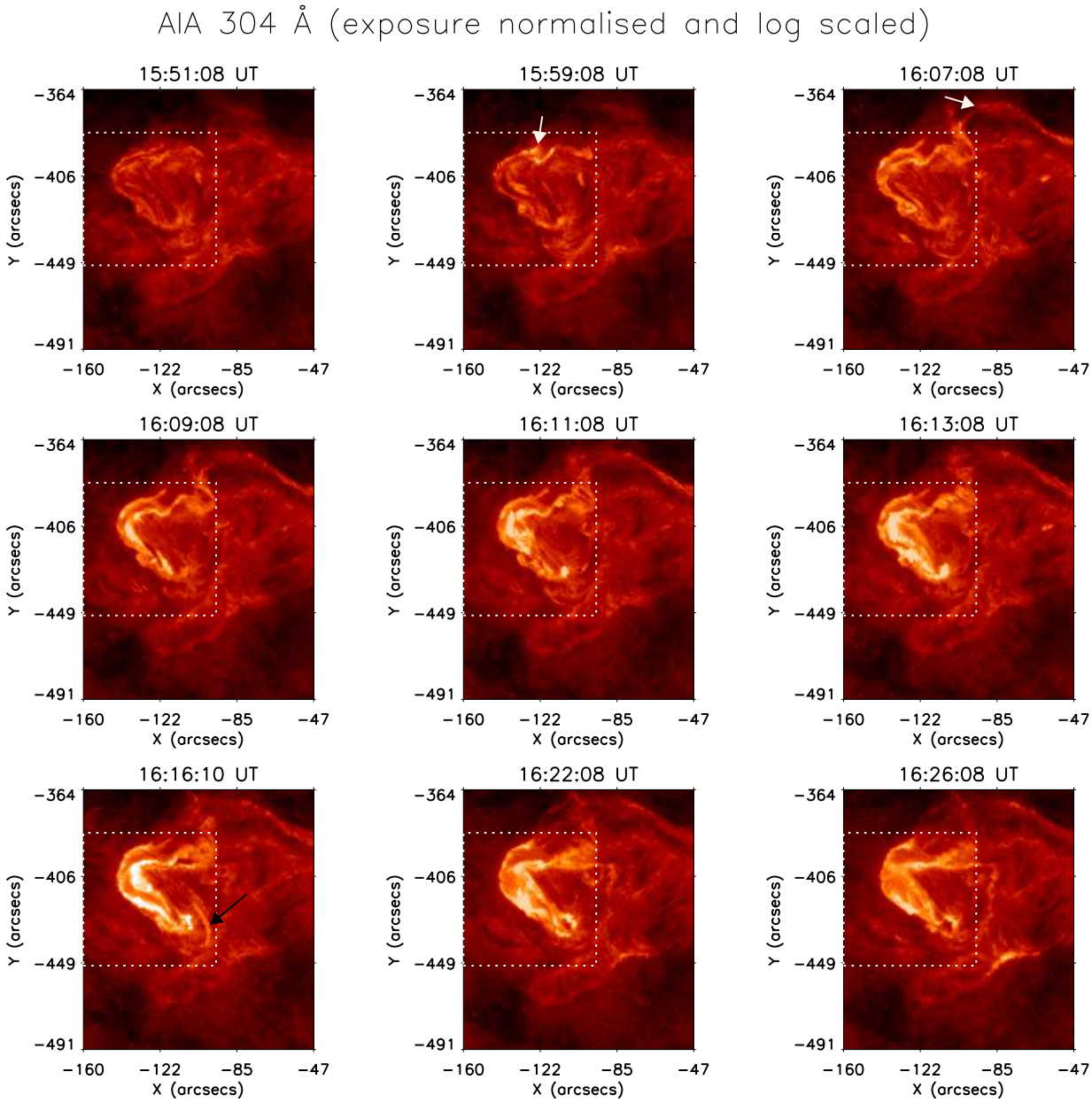

Fig. 9. The flare region in AIA He II 304 Å channel. The arrow at 15:59 UT indicates the first coronal eruption. The arrow at 16:07 UT denotes a rising loop. The arrow at 16:16 UT indicates the erupting filament seen in emission. The IBIS field of view is indicted as dotted lines. Animation of the full cadence images is available on line.

channels show a very sharp increase with the two AIA channels having their peak emission at 16:14 UT followed by the AIA 94 Å channel almost 5 min later. One of the features seen is the dip in the Hα blue-wing lightcurve which can be explained by the erupting filament (see the blue-wing lightcurve in Fig. 6, bottom panel). The same relative intensity variations in the line Hα centre and wings as in K1 and K2 are also observed here. Both the hard and soft X-ray emissions from GBM and GOES have the highest impulsive peak at 16:15 UT.

We also analysed the observations of the AIA 1600 Å channel, whose emission is dominated by continuum emission with some contribution by C IV lines (1548 Å and 1550 Å). Although the filament is not been seen in 1600 Å, the emission in the flare kernels seen in this channel shows similar evolution to that seen in the 304 Å channel.

3.3. Hα spectroscopy study (blue/red asymmetry)

Spectroscopic analysis of the solar chromosphere, for example Hα line profile analysis, provides crucial information for understanding the impact of the energy release during solar and stellar flares on the atmosphere. Thanks to the IBIS Hα line profile observations, we are able to report on this line profile evolution during various phases of a solar flare. This can help to identify the mechanism of energy transfer towards the lower atmosphere (i.e. the chromosphere, as discussed in the Introduction). Fig. A.1 (online material) presents the average Hα line profiles from a 5×5 px^2 (0.5″×0.5″) box in the centre of kernel K1 (described

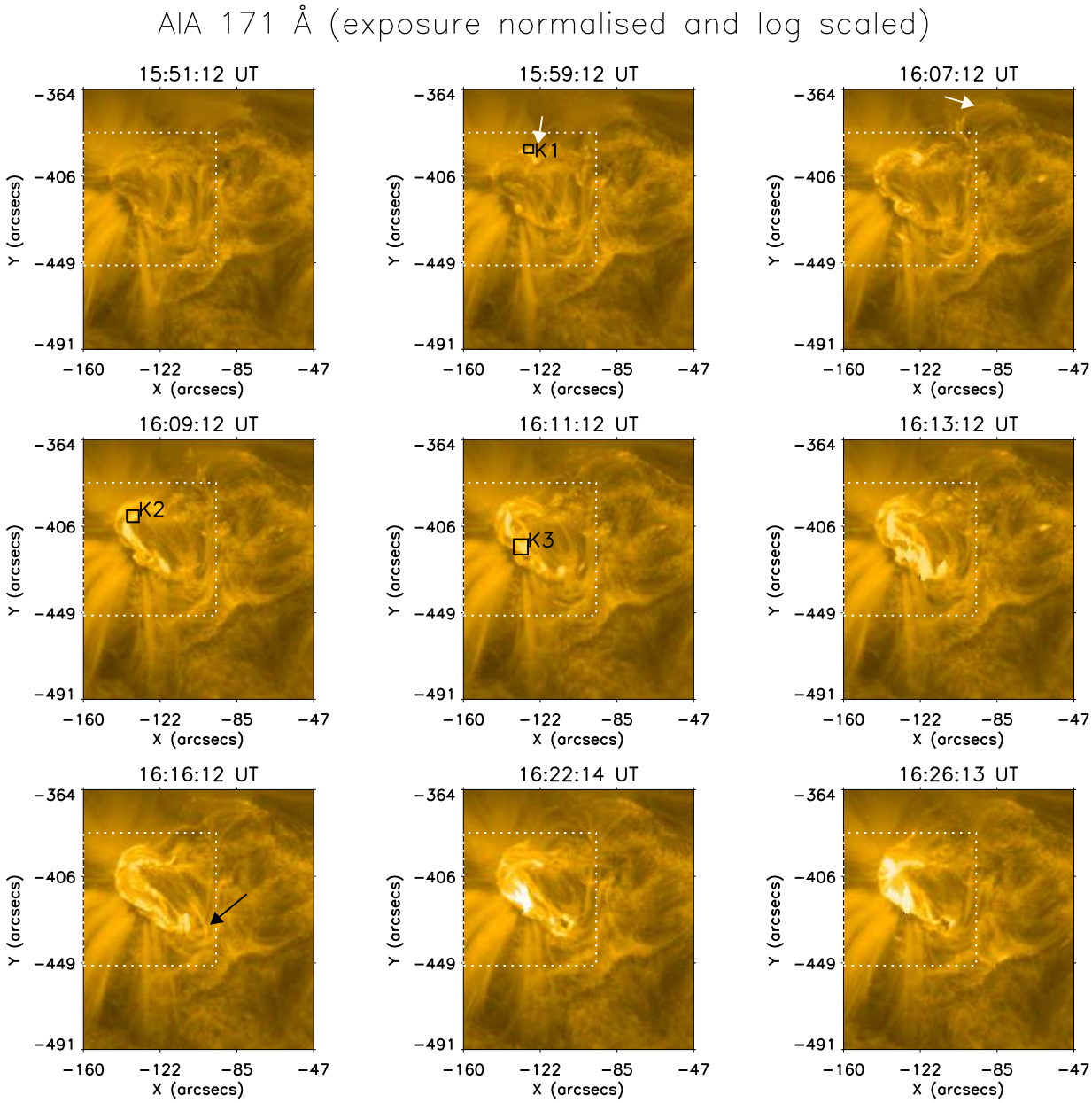

Fig. 10. As Fig. 9, showing the flare region seen in the AIA Fe x 171 Å channel. The three kernels (K1, K2, and K3; see text for details) are denoted in the images at 15:59 UT, 16:09 UT, and 16:11 UT, respectively.

in detail in Section 3.2). Consistent with the lightcurve of this kernel (see Fig. 6, top panel), the corresponding Hα line profiles show an enhancement in the line centre starting at 15:53 UT. Please note that the far wings of Hα are considered optically thin (Ichimoto & Kurokawa 1984) and the response there can be attributed to Doppler shifts rather than to the optical thickness of the line. We found that the increase in the line centre emission precedes the emission increase in the line wings by 5 mins. This is also clearly visible in the line profiles shown in Fig. A.1. If the emission in the line centre is assumed to come entirely from heating and the response in the far line wings from Doppler shifts, the delay would represent the time between the heating (either from energetic particles or thermal conduction) and the chromospheric condensation down-flow registered in the chromosphere. No blue asymmetry was detected in this ribbon. The profiles show a very minor reversal from absorption to emission, possibly because this ribbon was too weak, suggesting low energy release. This is also confirmed by the weak hard and soft X-ray emission registered after 15:45 UT until 16:09 UT by GBM and GOES, respectively (see Fig. 5), defined as phase 1 of the flare evolution. As discussed by Canfield et al. (1984), the Hα line width is also an important indicator of the heating mechanism during a flare (see Section 1 for details). We calculated the line width of those Hα line profiles that can be well fitted by a single Gaussian function. The results are shown in Fig. A.1. The full width at half maximum (FWHM) of Hα increases from 1.57 Å at 15:58 UT to 2.04 Å at 16:04 UT, and then decreases to 1.67 Å at 16:07 UT. However, the line width does not always increase, and it decreases at the earlier stage, e.g. at 15:59 UT, 16:00 UT, and 16:01 UT. The complex evolution of the Hα line profiles suggests that possibly several heating mechanisms are at work in this ribbon.

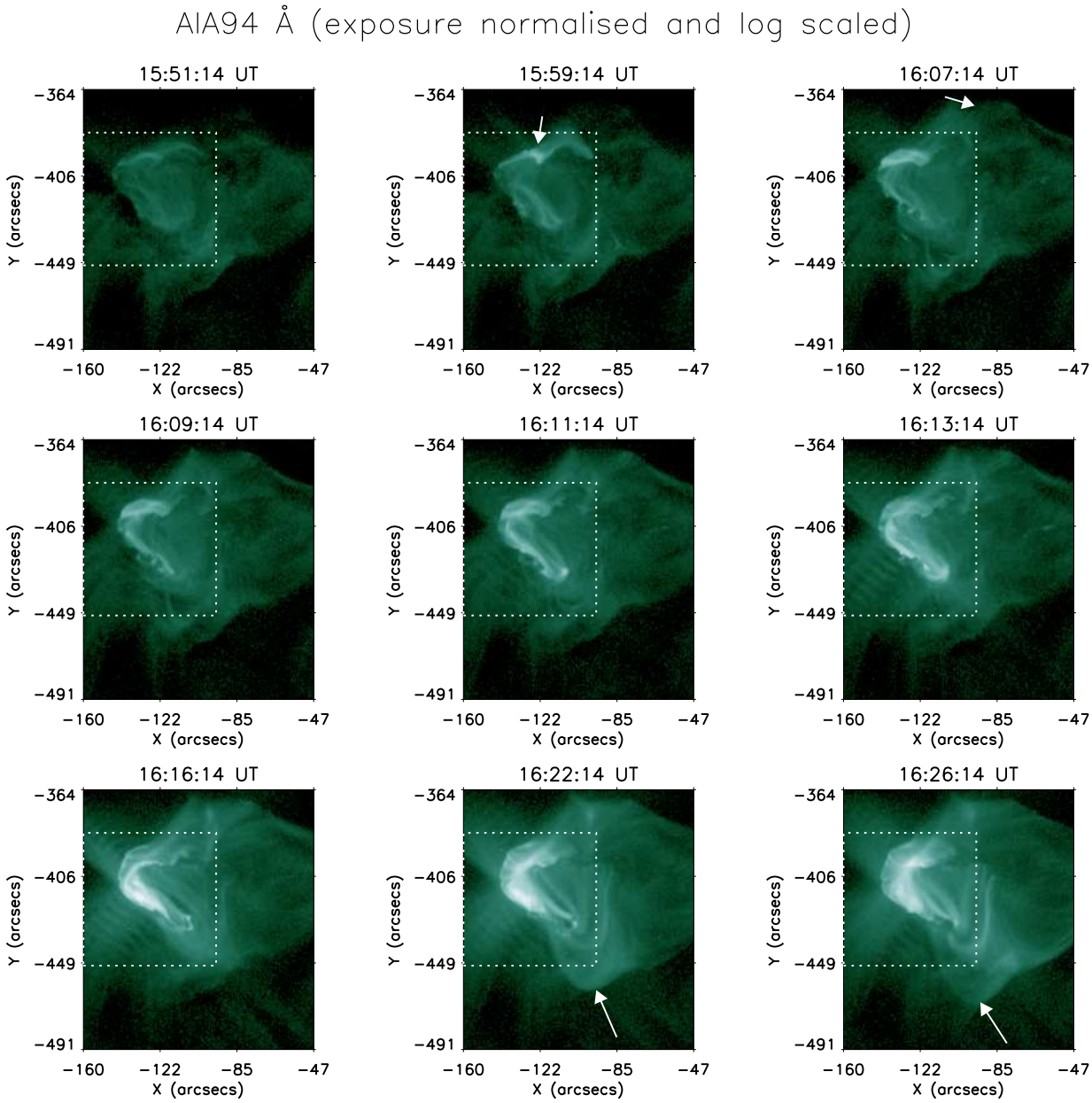

Fig. 11. As Fig. 9, showing the AIA Fe XVIII 94 Å channel. The arrows marked in the images at 16:22 UT and 16:26 UT show the rising coronal loops indicating the initiation of the CME.

The evolution of the Hα line profiles taken from the centre of K2 is presented in Fig. A.2 (online material). The emission increase in the line centre begins at 16:03 UT. The energy released in this kernel (during the second phase of the flare) is stronger than K1, producing clear emission profiles. The first such profile, together with the first sign of red asymmetry, is seen at ~16:08:52 UT which also coincides with the beginning of the impulsive peak seen in the hard and soft X-ray emission (Fig 5). The delay between the emission increase in the line centre and the occurrence of the red asymmetry as determined in the far wings of Hα is again ~5 minutes, as in K1. The second reversal into emission of the Hα line profile appears during the strongest impulsive peak of the flare from 16:16 UT to 16:25 UT. This supports the interpretation that non-thermal electron beams are mostly responsible for the chromospheric heating. Red asymmetry is clearly present in the emission line profiles (e.g. 16:09:27 UT, 16:09:45 UT, 16:18:36 UT, etc). Again, no blue asymmetry is found in this kernel. From 16:14 UT to 16:15 UT, Hα line profiles in this kernel turn back to absorption due to the rising filament which crosses the area of this kernel. From 16:03 UT to 16:35 UT, the line width in this kernel does not exceed 1.95 Å. Comparing this to 1.74 Å at 16:03 UT when the ribbon starts flaring, the small increase in the line width suggests that non-thermal electron beam and thermal conduction work together to heat this kernel.

Fig. A.3 (online material) then shows the Hα line profile evolution in K3 (located in the main ribbon) during the third impulsive peak. The emission in the line centre in this kernel starts increasing at ~16:05 UT. The first emission profile is recorded shortly before 16:14 and lasts until 16:23 UT, i.e. 9 mins. The red asymmetry appears from 16:11 UT to 16:17 UT. Thus, the delay between the line centre emission and the red asymmetry

is ~6 mins. Blue asymmetry is observed after 16:30 UT. However, we find that it is not associated with the ribbon but with the red-wing absorption from the down-falling filament material.

In order to study the asymmetry in the Hα line profiles over the whole flaring region, we developed an algorithm to automatically detect these phenomena by comparing the total intensity of three points of wavelength in the blue and red wings of the line profiles. The difference between the total intensity of the blue and red wings is then calculated. Differences that exceed three sigma are considered to be a wing asymmetry. Furthermore, we randomly selected more than one hundred samples in the flare ribbon and visually examined their line profiles in order to confirm that the detection from the automatic procedure is reliable. We found that blue asymmetry is only associated with the dynamics of the filament, and no blue asymmetry is identified in the ribbons where only red asymmetry is found. We note that significant red asymmetry is also associated with the filament plasmas. This result is consistent with Canfield et al. (1990b) and supports their suggestion for a strong connection between a Hα blue asymmetry and dynamic filaments.

3.4. Magnetic field evolution

We used HMI/SDO line-of-sight magnetograms to study the magnetic field evolution before and during the flare. The left panel of Fig. 3 shows a HMI magnetogram at 16:14 UT. As mentioned above, the filament destabilisation is possibly due to the new positive flux emergence. Unfortunately, the resolution and sensitivity of the HMI magnetograms are not sufficient to establish with enough certainty where the crucial emergence has taken place. Nevertheless, the increased activity in one of the filament footpoints (see Section 3.1) leads to the filament destabilisation and following eruption. The lightcurves of the positive and the negative flux reveal a very high rate of magnetic flux cancellation of 1.34×10^{16} Mx s^{-1} (see the definition of cancellation rate in Huang et al. 2012). This cancellation rate is two orders of magnitudes larger than that found in Huang et al. (2012) for an X-ray jet, and is consistent with their suggestion that a more explosive event in the solar atmosphere is likely to be associated with a larger magnetic cancellation rate. This also suggests that flux cancellation might drive both small- and large-scale explosive events in the solar atmosphere.

3.5. CME association

The CME initiation was recorded by both EUVI instruments on STEREO A and B thanks to the suitable position angle of the two satellites. By using an image difference technique, we analysed the CME lift-off in the EUVI A and B images. The signature of the ejected material is very faint but, nevertheless, clear enough to identify the erupting material. A coronal mass ejection was registered by LASCO C2 on board SoHO, and by COR1 and COR2 on board the STEREO Ahead and Behind spacecrafts. The CME was first registered in SECCHI COR1 at 16:15 UT (Fig. 12). It propagated with an average speed of 367 km s^{-1}(minimum 250 km s^{-1} and maximum 595 km s^{-1}) as measured in SECCHI COR2 (from CACTus automatic measurements[1]). We measured an angular width of the CME of 59° determined in SECCHI COR2 (CACTus gives 66°). Two clouds are seen forming the CME, with the first one appearing at approximately 16:15 UT followed by the second one displaced more to the south between 16:25 UT and 16:30 UT. The two parts of the CME reflect the complexity of the flare event described above. We can speculate that the two separate clouds ejected with a time difference of ~10–15 mins (note the 5 min cadence of the images) coincides with the two strong impulsive peaks recorded during the flare. The first cloud initiats in the region above kernel K1 while the second forms during the next two phases.

[1] http://sidc.oma.be/cactus/

4. Summary

In the present study we analysed multi-instrument observations of a GOES C4.3 solar flare with filament destabilisation and eruption that occurred in NOAA 11123 on 2010 November 11. As a result of this activity a coronal mass ejection formed. We used a unique combination of ground- and space-based spectral and imaging observations to explore in great detail both temporally and spatially the small-scale evolution of all three phenomena. The main results can be summarised as follows:

We found that the filament destabilisation and eruption was the main trigger for the flaring activity. A surge-like event with a circular ribbon at the filament footpoint was determined to be the trigger of the filament destabilisation. Draining in one of the footpoints of the filament was identified as the precursor for the eruption.

HMI line-of-sight magnetograms revealed magnetic flux emergence prior to the filament destabilisation followed by a high rate of flux cancellation of 1.34×10^{16} Mx s^{-1} during the flare activity.

GBM/Fermi and GOES lightcurves reveal a complex flare evolution with three phases with different energetics. Each phase was associated with a particular chromospheric (three separate ribbon formations) and coronal activity (brightenings and loop ejections). Three kernels were studied in detail for each ribbon. In each kernel the intensity increase in the Hα line centre is much stronger than the emission increase in the line wings. This is consistent with the latest simulations by Kašparová et al. (2009) showing that non-thermal electron beams result in emission enhancement and have only a small contribution to the Doppler wings. In all three kernels, the delay between the line centre emission increase and the red asymmetry was around 5–6 mins. We have to point out that the interpretation of the Hα line is not straightforward because of the optical thickness and complex formation of this line.

No reversal to emission in the Hα was found during the weakest phase of the flare, which is consistent with the hard X-ray emission which registered the event only in the 4.2 - 14.6 keV range. A second phase is related to the first impulsive peak registered in hard (up to 25 keV) and soft X-rays. During this phase Hα line emission profiles were observed. The strongest impulsive peak produced hard X-ray emission in the range of 25 – 50 keV, but most of the hard X-ray flux comes from the lowest energy band of 4.2 to 15 keV. In the flare ribbons, only red asymmetry is found during all three phases. In contrast, the blue asymmetry is entirely associated with the dynamic filament.

The filament-eruption/flare event produces a narrow coronal mass ejection comprising two clouds released with a time difference of approximately 10 min which reflects the complexity of the energy release during this flare. The filament displays a failed eruption, but presumably some of the filament material escaped and so could not be detected in the fields of view or temperature ranges of the available instrumentation. While the whole filament appears to have been destabilised only part of it had erupted.

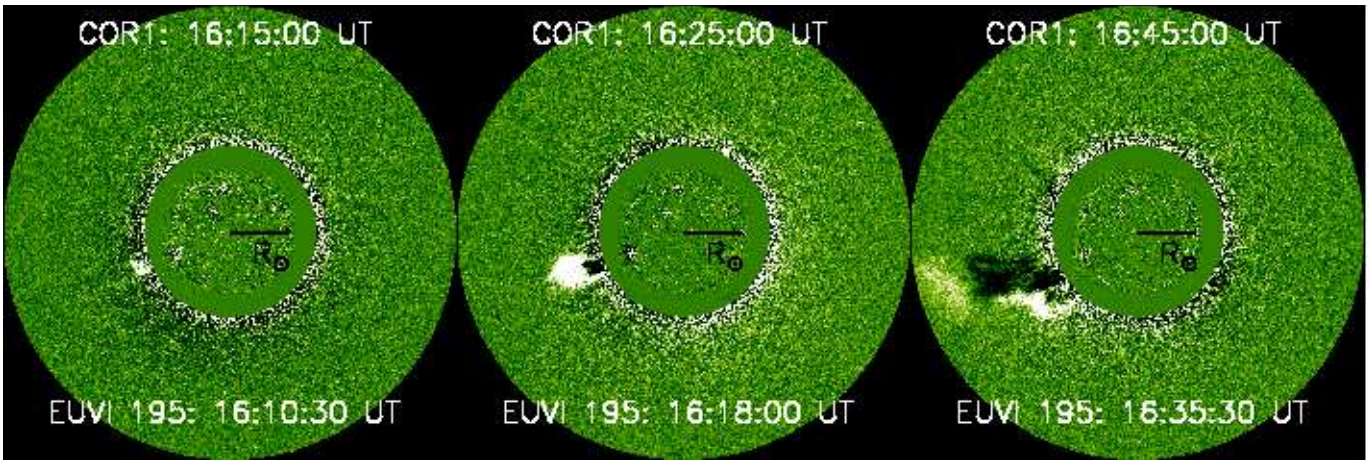

Fig. 12. Combination of SECCHI/COR1 and EUVI 195 Å Ahead images of the CME caused by the filament/flare sequence of events.

The data presented in this study will be further explored both for comparison with data driven three-dimensional magneto-hydrodynamic numerical simulations as well as Hα line profile calculations. A separate study will analyse in more detail the coronal mass ejection detected during this event.

Acknowledgements. This research is supported by the China 973 program 2012CB825601, and the National Natural Science Foundation of China under contracts: 41274178, 40904047, 41174154, 41274176. Research at the Armagh Observatory is grant-aided by the N. Ireland Dept. of Culture, Arts and Leisure. We thank PATT T&S for their support, and are grateful for support from STFC grant ST/J001082/1 and the Leverhulme Trust. We thank the National Solar Observatory Sacramento Peak for their hospitality in particular Doug Gilliam for his help during the observations. We thank Dr. Gianna Cauzzi for her great help with the IBIS data reduction. We would also like to thank Friedrich Wöger for his KISIP code. We also thank very much Kim Tolbert for her great support for handling the Fermi data. We thank Klaus Galsgaard for the careful reading and constructive suggestions on the manuscript. AIA and HMI data is courtesy of SDO (NASA). We would like to thank the anonymous referee for his/her critical and constructive comments. We thank Marilena Mierla for the helpful discussion on the coronal mass ejection.

References

Alexander, D., Liu, R., & Gilbert, H. R. 2006, ApJ, 653, 719
Allred, J. C., Hawley, S. L., Abbett, W. P., & Carlsson, M. 2005, ApJ, 630, 573
Asai, A., Ichimoto, K., Kita, R., Kurokawa, H., & Shibata, K. 2012, PASJ, 64, 20
Benz, A. O. 2008, Living Reviews in Solar Physics, 5
Canfield, R. C., Gunkler, T. A., & Ricchiazzi, P. J. 1984, ApJ, 282, 296
Canfield, R. C., Metcalf, T. R., Zarro, D. M., & Lemen, J. R. 1990a, ApJ, 348, 333
Canfield, R. C., Penn, M. J., Wulser, J.-P., & Kiplinger, A. L. 1990b, ApJ, 363, 318
Canfield, R. C. & Reardon, K. P. 1998, Sol. Phys., 182, 145
Carmichael, H. 1964, NASA Special Publication, 50, 451
Cauzzi, G., Reardon, K., Rutten, R. J., Tritschler, A., & Uitenbroek, H. 2009, A&A, 503, 577
Cavallini, F. 2006, Sol. Phys., 236, 415
Chen, P. F. 2011, Living Reviews in Solar Physics, 8, 1
Cheng, J. X., Ding, M. D., & Li, J. P. 2006, ApJ, 653, 733
Cirigliano, D., Vial, J.-C., & Rovira, M. 2004, Sol. Phys., 223, 95
Del Zanna, G., O'Dwyer, B., & Mason, H. E. 2011, A&A, 535, A46
Deng, N., Tritschler, A., Jing, J., et al. 2013, ApJ, 769, 112
Engvold, O., Jakobsson, H., Tandberg-Hanssen, E., Gurman, J. B., & Moses, D. 2001, Sol. Phys., 202, 293
Fang, C., Henoux, J. C., & Gan, W. Q. 1993, A&A, 274, 917
Feynman, J. & Martin, S. F. 1995, J. Geophys. Res., 100, 3355
Fletcher, L., Dennis, B. R., Hudson, H. S., et al. 2011, Space Sci. Rev., 159, 19
Fletcher, L. & Hudson, H. S. 2008, ApJ, 675, 1645
Gibson, S. E., Foster, D., Burkepile, J., de Toma, G., & Stanger, A. 2006, ApJ, 641, 590
Gilbert, H. R., Holzer, T. E., Burkepile, J. T., & Hundhausen, A. J. 2000, ApJ, 537, 503
Graeter, M. & Kucera, T. A. 1992, Sol. Phys., 141, 91
Harrison, R. A., Waggett, P. W., Bentley, R. D., et al. 1985, Sol. Phys., 97, 387
Heinzel, P., Karlicky, M., Kotrc, P., & Svestka, Z. 1994, Sol. Phys., 152, 393
Hirayama, T. 1974, Sol. Phys., 34, 323
Howard, R. A., Moses, J. D., Vourlidas, A., et al. 2008, Space Sci. Rev., 136, 67
Huang, Z., Madjarska, M. S., Doyle, J. G., & Lamb, D. A. 2012, A&A, 548, A62
Hudson, H. S. 2007, in Astronomical Society of the Pacific Conference Series, Vol. 368, The Physics of Chromospheric Plasmas, ed. P. Heinzel, I. Dorotovič, & R. J. Rutten, 365
Ichimoto, K. & Kurokawa, H. 1984, Sol. Phys., 93, 105
Ji, G. P., Kurokawa, H., Fang, C., & Huang, Y. R. 1994, Sol. Phys., 149, 195
Jiang, Y. C., Chen, H. D., Li, K. J., Shen, Y. D., & Yang, L. H. 2007, A&A, 469, 331
Kaiser, M. L., Kucera, T. A., Davila, J. M., et al. 2008, Space Sci. Rev., 136, 5
Kašparová, J., Varady, M., Heinzel, P., Karlický, M., & Moravec, Z. 2009, A&A, 499, 923
Kopp, R. A. & Pneuman, G. W. 1976, Sol. Phys., 50, 85
Kucera, T. A. & Landi, E. 2006, ApJ, 645, 1525
Kucera, T. A. & Landi, E. 2008, ApJ, 673, 611
Lemen, J. R., Title, A. M., Akin, D. J., et al. 2012, Sol. Phys., 275, 17
Liu, Y., Hoeksema, J. T., Scherrer, P. H., et al. 2012, Sol. Phys., 279, 295
Magara, T., Mineshige, S., Yokoyama, T., & Shibata, K. 1996, ApJ, 466, 1054
Martin, S. F. 1980, Sol. Phys., 68, 217
Meegan, C., Lichti, G., Bhat, P. N., et al. 2009, ApJ, 702, 791
O'Dwyer, B., Del Zanna, G., Mason, H. E., Weber, M. A., & Tripathi, D. 2010, A&A, 521, A21
Pesnell, W. D., Thompson, B. J., & Chamberlin, P. C. 2012, Sol. Phys., 275, 3
Reardon, K. P. & Cavallini, F. 2008, A&A, 481, 897
Russell, A. J. B. & Fletcher, L. 2013, ApJ, 765, 81
Saint-Hilaire, P. & Benz, A. O. 2005, A&A, 435, 743
Schou, J., Scherrer, P. H., Bush, R. I., et al. 2012, Sol. Phys., 275, 229
Shibata, K. & Magara, T. 2011, Living Reviews in Solar Physics, 8
Sturrock, P. A. 1966, Nature, 211, 695
Tandberg-Hanssen, E., ed. 1995, Astrophysics and Space Science Library, Vol. 199, The nature of solar prominences
Tang, F. 1983, Sol. Phys., 83, 15
Švestka, Z. 1976, Solar Flare (Springer)
Švestka, Z., Kopecký, M., & Blaha, M. 1962, Bulletin of the Astronomical Institutes of Czechoslovakia, 13, 37
Wöger, F., von der Lühe, O., & Reardon, K. 2008, A&A, 488, 375
Zarro, D. M., Canfield, R. C., Metcalf, T. R., & Strong, K. T. 1988, ApJ, 324, 582

Appendix A: Online material

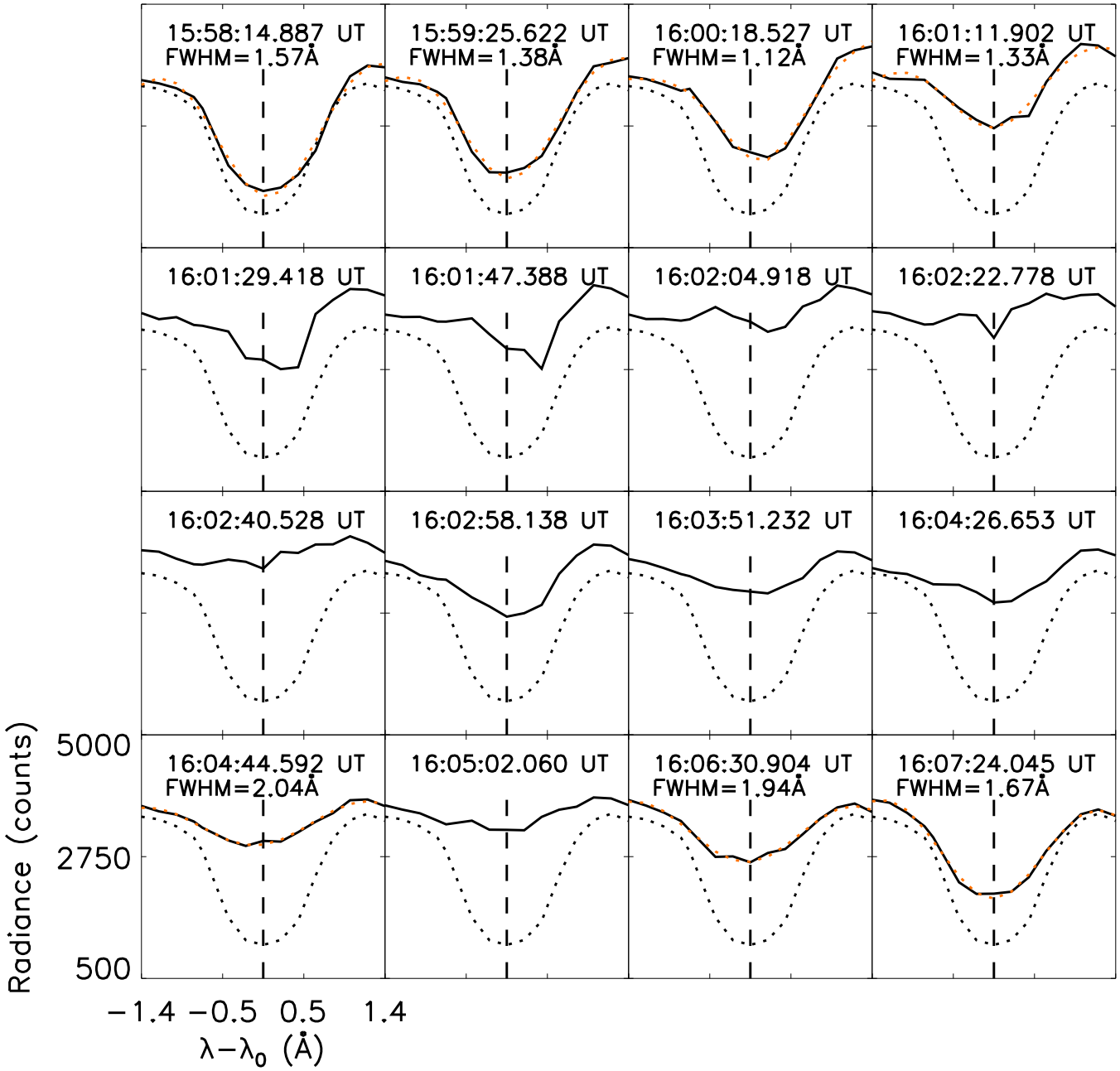

Fig. A.1. Hα line profiles (solid lines) from the kernel K1 together with a reference profile (black dotted lines) taken from a quiet region at the bottom-left corner of the field of view. The line centre λ_0 is denoted by dashed lines. FWHM of those profiles that can fitted by a single-Gaussian function are noted accordingly, and their fitting Gaussian profiles (orange dotted lines) are overplotted.

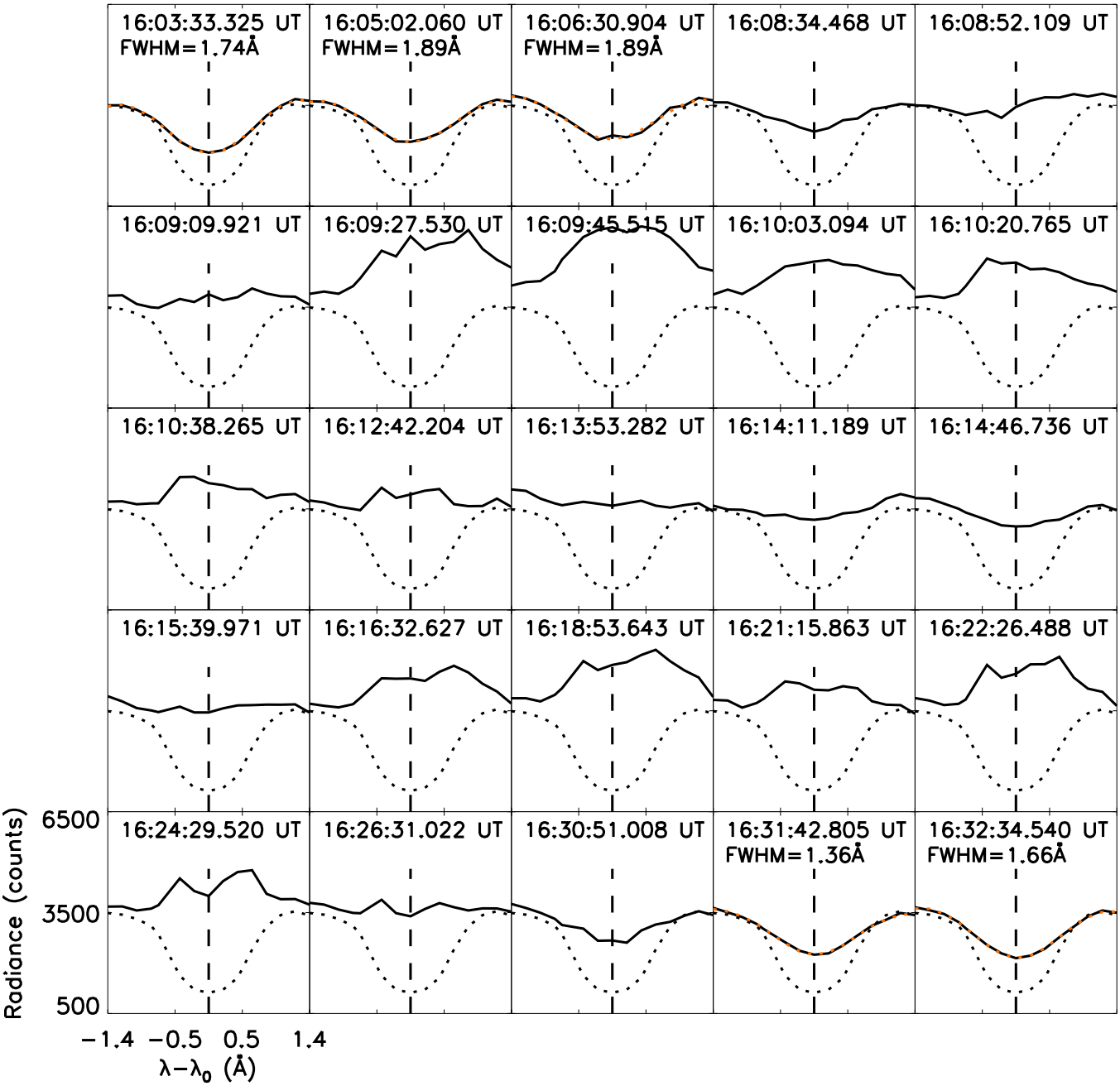

Fig. A.2. As Fig. A.1, the evolution of Hα line profiles from the kernel K2.

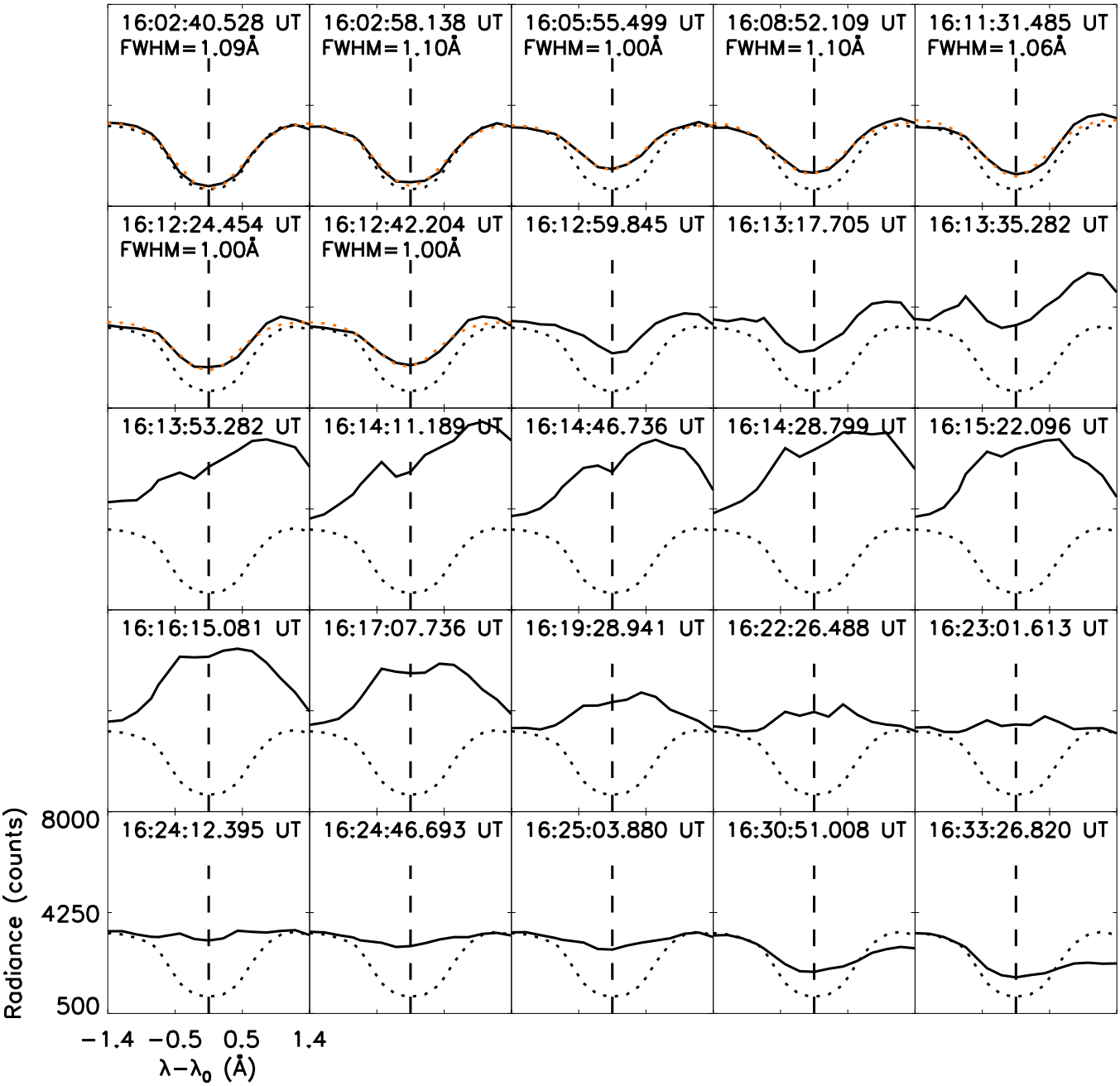

Fig. A.3. As Fig. A.1, the evolution of Hα line profiles from the kernel K3.

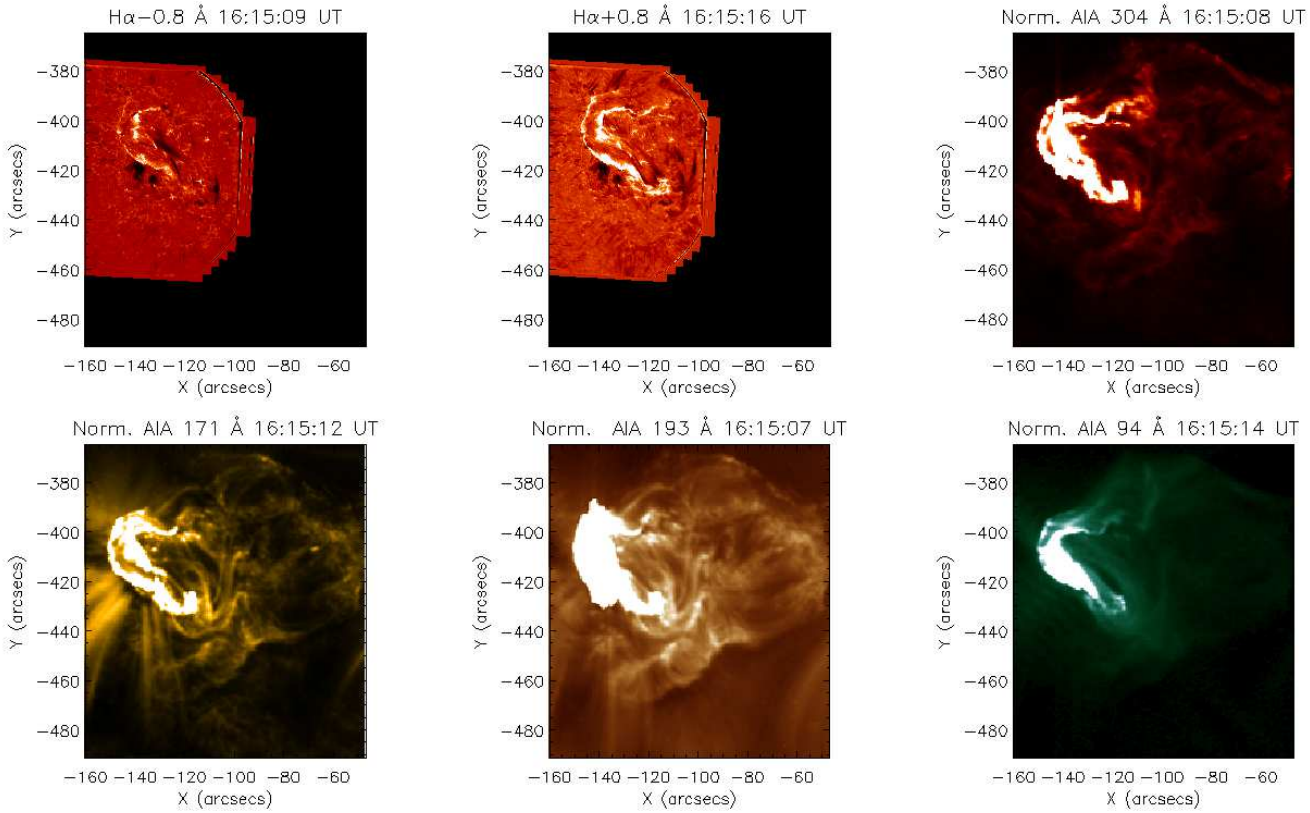

Fig. A.4. An animation displaying the evolution of the flare seen in six different channels. Top-left: Hα – 0.8 Å; top-middle: Hα + 0.8 Å; top-right: AIA 304 Å; bottom-left: AIA 171 Å; bottom-middle: AIA 193 Å; bottom-right: AIA 94 Å.